Inorganic Chemistry

pubs.acs.org/IC

Article

Tuning the Properties of Azadipyrromethene-Based Near-Infrared Dyes Using Intramolecular BO Chelation and Peripheral Substitutions

Jayvic C. Jimenez, Zehao Zhou, Arnold L. Rheingold, Shane M. Parker, and Geneviève Sauvé*

Cite This: https://doi.org/10.1021/acs.inorgchem.1c01597

Read Online

ACCESS | Metrics & More | Article Recommendations | Supporting Information

ABSTRACT: Tetraphenylazadipyrromethenes (ADPs) are attractive near-infrared (NIR) dyes because of their simple synthesis and exceptional optical and electronic properties. The typical BF_2 and less explored intramolecular BO coordination planarize the molecule, making them promising π-conjugated materials for organic electronic applications. However, their use has been mostly limited to vacuum-deposited devices. To improve the properties, we synthesized and characterized a series of ADP complexes and used density functional theory calculations to further explain the properties. Hexyloxy solubilizing groups increase the complexes' solubility in organic solvents and enable film formation from solution. Phenylethynyls at the pyrrolic positions extend π conjugation, red-shift absorption and emission peaks, and increase the ionization potential (IP) and electron affinity. When the properties of complexes with hexyloxy and phenyethynyl substitutions are compared, the BO complex is more planar and has a smaller IP than the corresponding BF_2 complex because of increased electron density on the proximal phenyls. The BO complex has an unusual combination of properties: a solution λ_{max} of 781 nm, emission at 805 nm, a small Stokes shift, and a quantum yield of 6%. It forms transparent films with a low optical gap of 1.22 eV. This new complex is a promising candidate for transparent solar cells and NIR photodetectors.

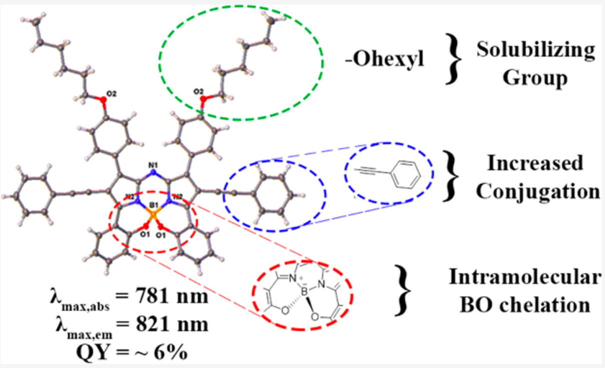

■ INTRODUCTION

Near-infrared (NIR) dyes are of great interest for many applications including biological sensing and imaging, photodynamic therapy, NIR photodetection, and solar energy conversion.[1−4] In particular, dipyrromethene- and azadipyrromethene-based dyes have attracted a lot of attention because of their tunable and strong absorption in the visible-to-NIR range and fluorescence properties.[5−8] These are π-conjugated bidentate ligands that are typically coordinated with difluoroboryl (BF_2, known as BODIPY and aza-BODIPY) but can also be coordinated with other Group 13 elements and transition metals.[5,9,10] Approaches to red-shifting the optical properties include introducing electron-rich/electron-poor functional groups to create a push−pull effect, extending conjugation, and rigidifying the molecule via fused rings.[11,12] One underexplored strategy to red-shifting the absorption spectra is to use intramolecular BO bonds. Here, hydroxide groups are added to the ortho position of the proximal phenyls, resulting in a tetradentate $N_2O_2{}^{n-1}$ ligand that can coordinate with transition metals or Group 13 elements such as boron, thus rigidifying the structure by restricting the proximal phenyls from rotating.[13,14]

Azadipyrromethenes differ from dipyrromethenes in that the carbon that connects the two pyrrole rings is replaced with nitrogen. This substitution red-shifts the absorption spectra and increases the electron affinity (EA). The easiest ligand to synthesize is the 1,3,5,7-tetraphenylazadipyrromethene (ADP), shown in Figure 1.[15] This ligand has an absorption peak at 600 nm in solution. Coordination with BF_2 red-shifts the absorption peak to 650 nm and increases the emission quantum yields (QYs) and EA.[12,16] Using intramolecular BO complexation further red-shifts absorption of the unsubstituted ADP to 728 nm.[17,18] Extending the conjugation of aza-BODIPY [or BF_2(ADP) using our nomenclature] with phenylethynyl groups at the pyrrolic positions also red-shifts the absorption significantly to 732 nm.[19] An ADP molecule that combines the effect of BO intramolecular coordination with extended conjugation of phenylethynyl groups has not been published to our knowledge, but one would expect further red-shifting.

Received: June 2, 2021

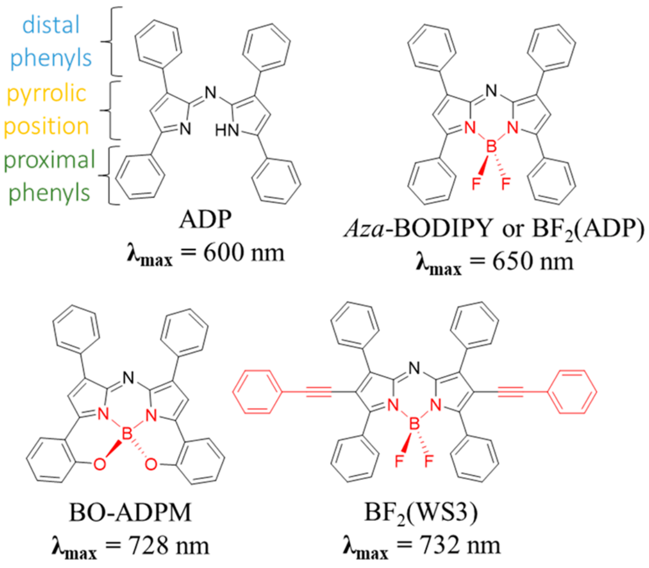

Figure 1. Molecular structure of ADP bearing chemically modifiable positions: proximal phenyls, distal phenyls, pyrrolic positions, and chelation. Some approaches to red-shift the absorption spectra are as follows: BF_2 chelation, intramolecular BO chelation, and a combination of BF_2 chelation and extension of conjugation with phenylethynyls at the pyrrolic positions.

In terms of applications, BF_2-chelated ADPs have been explored for several biological applications, as well as active materials in organic solar cells.[20,21] The BO intramolecular bonds are unstable to water and alcohols because these can compete with intramolecular boron coordination. This limits its use in biological applications but is still of interest for organic electronic applications such as photovoltaics and photodetectors, where water is usually avoided. For example, BO-chelated ADPs were successfully used in vacuum-deposited organic solar cells.[22,23] In terms of solar cell applications, BF_2- and BO-chelated ADPs have mostly been limited to vacuum-deposited devices because of low solubility in organic solvents. One exception is a report where NIR-absorbing benzannulated aza-BODIPY dyes were used in ternary solution-processed solar cells to increase NIR solar harvesting.[24] Our group has tested BF_2(ADP) and BF_2(WS3) (shown in Figure 1) in organic solar cells by blending with the common donor poly(3hexylthiophene) in a 1:1 ratio. In our hands, the cells did not show any significant photovoltaic effect, most likely because of poor film formation and unfavorable blend morphology.[19] To enable these systems to form good films and work in solution-processable solar cells, it is necessary to introduce solubilizing groups. While functionalization with hydrophilic groups has been explored to increase the water solubility of ADP-based complexes for biological applications,[25,26] we are not aware of any reports exploring the use of hydrophobic solubilizing groups on the BF_2- or BO-chelated ADP complexes to enable their use in solution-processed organic electronic devices.

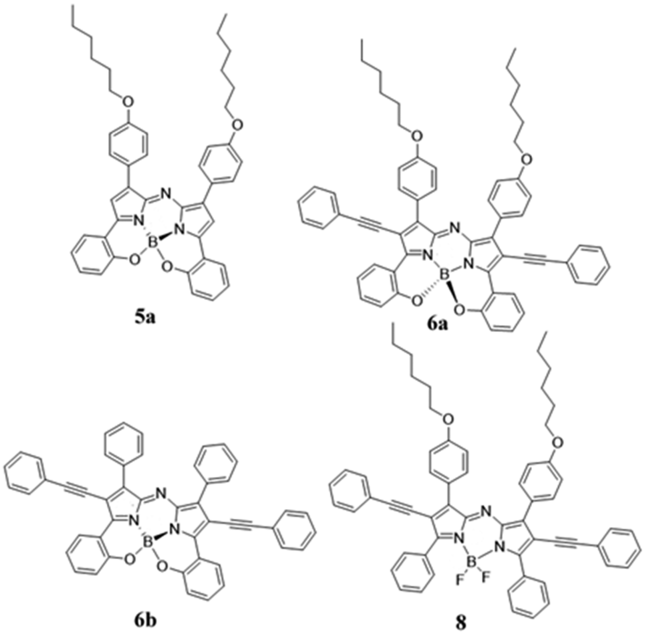

Figure 2. New complexes synthesized in this work.

Here, we have synthesized and characterized four new complexes of ADP, shown in Figure 2. This series of molecules was chosen to look at the effect of three different peripheral substitutions on the properties of BO-chelated ADP: hexyloxy solubilizing groups at the para position of the distal phenyls (**5a**), hexyloxy on the distal phenyls plus phenylethynyls at the pyrrolic positions (**6a**), and phenylethynyls at the pyrrolic position (**6b**). Also, to directly compare the effect of coordination for molecules with phenylethynyls at the pyrrolic position, we synthesized an analogue of **6a**, molecule **8**, and used the previously published analogue of **6b**, BF_2(WS3).[19] The thermal, structural, optical, and electrochemical properties of the four newly synthesized complexes were examined, and density functional theory (DFT) calculations were used to further understand the effect of these chemical modifications on the properties.

■ RESULTS AND DISCUSSION

Synthesis. Synthesis of the complexes is shown in Scheme 1. First, the chalcones **3a** and **3b** were synthesized by grinding the appropriate starting materials **1** and **2** in a mortar and pestle similar to the published procedure.[27] The crude chalcones were recrystallized in methanol (MeOH), resulting in either a bright-yellow crystalline solid with ~45% yield for the Y = OH substitution or an off-white crystalline solid with ~64% yield for the Y = H substitution. The free ligands **4a**–**4c** were obtained by the Michael addition of nitromethane, followed by annulation with ammonium acetate in 1-butanol.[28] The free ligands were washed with MeOH and isolated in moderate yields of ~36–42%.

While reaction of the free ligands with boron trifluoride usually forms a BF_2 complex, the presence of an *o*-phenolic group in **4a** and **4b** favors formation of the intramolecular borate (Scheme 1B; called BO in this work).[17] The BO complexes can withstand Stille coupling conditions to append the phenylethynyl groups at the pyrrolic positions, giving **6a** and **6b**. The BF_2 complex analogue to **6a** was also synthesized by installing phenylethynyl groups at the pyrrolic positions of **4c**, followed by reaction with boron fluoride to give complex **8**. The final complexes were successfully purified by recrystallization. All complexes were characterized by ^{1}H and ^{13}C NMR to determine the chemical structure and matrix-assisted laser desorption ionization time-of-flight (MALDI-TOF) mass spectrometry to confirm the purity and molecular mass. The presence of tetrahedral boron in both BO and BF_2 complexes was confirmed by ^{11}B NMR, with a signal in the 0–2 ppm

Scheme 1. Synthesis of (A) ADP Compounds, (B) BO-Coordinated Complexes, and (C) the BF_2 Complex[a]

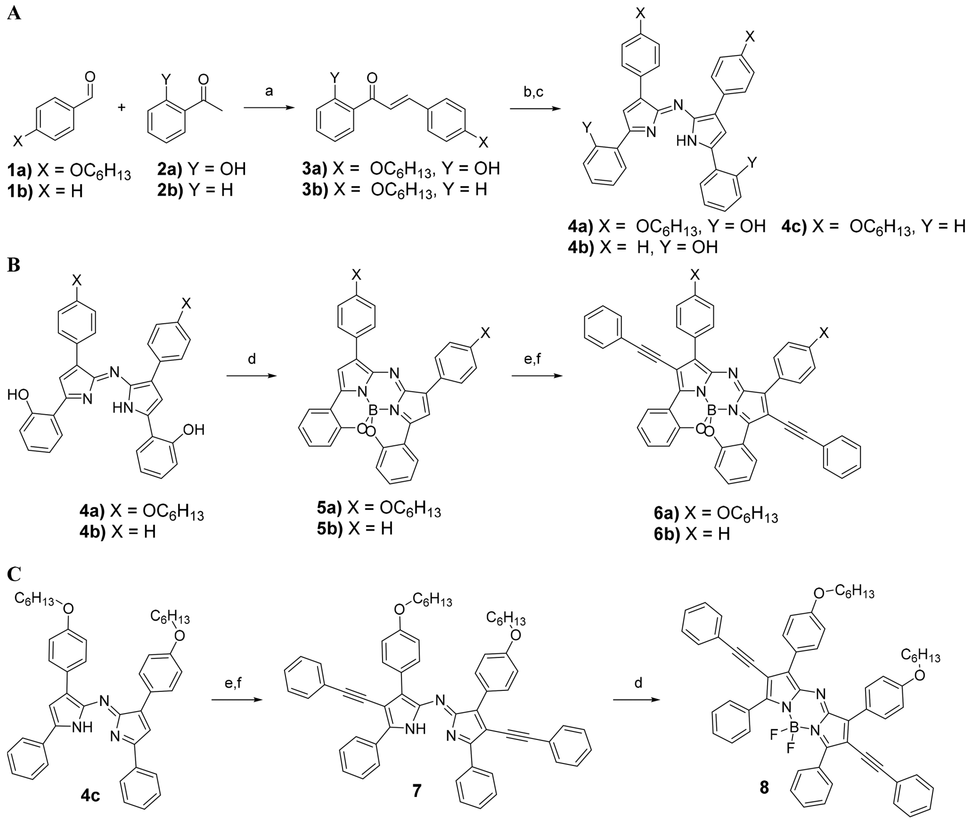

[a] (a) NaOH, ground, (b) $MeNO_2$, NEt_3 in MeOH at 90 °C, (c) ammonium acetate in 1-BuOH, (d) BF_3OEt_3 in toluene at 110 °C, (e) NIS in $CHCl_3$, and (f) $Pd(PPh_3)_4$ and tributyl(phenylethynyl)tin in xylenes at 150 °C.

range (a singlet for BO and a triplet for BF_2). The presence of fluorine in the BF_2 complex was confirmed by ^{19}F NMR, with a characteristic quartet signal around −130 ppm. All complexes are stable in air in the solid state. The BO complexes are stable in tetrahydrofuran (THF) or chlorinated solvents but tend to degrade in the presence of water or alcohol. In contrast, the BF_2 complex is generally stable in solution, even in the presence of water or alcohol.

Thermal Properties. Thermal properties were determined by thermogravimetric analysis (TGA; Figure S1 and Table S1) and differential scanning calorimetry (DSC; Figure 3). TGA indicates that all complexes are thermally stable, with 5% weight loss temperatures of >390 °C (see the Supporting Information). For DSC measurements, we analyzed crystals obtained from solvent diffusion in THF/MeOH, except for **6b**, which produced no resolvable crystals. To avoid sample decomposition, the samples were heated to a maximum of 350 °C, a temperature well below the 5% weight loss temperatures found by TGA. The DSC first heating cycles of crystals of **5a** and **6a** have weak and broad endothermic peaks at ∼180 and 210 °C, respectively, suggesting thermal motion corresponding to movement of the alkoxy solubilizing groups. Upon further heating, all complexes except **6b** exhibit a sharp melting peak, followed by a broad exothermic peak (marked with an asterisk). The melting temperatures were 236, 290, and 230 °C for **5a**, **6a**, and **8**, respectively. Complex **6b** (without solubilizing groups) shows only a sharp exothermic peak at 342 °C (marked with an asterisk) with no melting peak. This is expected because **6b** did not produce crystals suitable for X-ray diffraction (XRD). The solubilizing groups therefore facilitate crystallization. All four complexes do not show any thermal features during cooling (Figure S2), suggesting that they have assembled into a vitrified state during the endothermic phase of the heating and are not recrystallizing at the cooling rate used. A second heating cycle shown in Figure S2 shows the

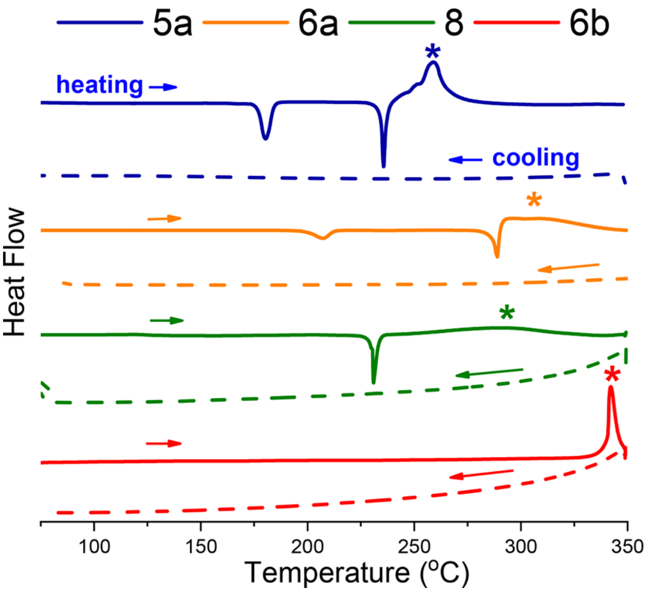

Figure 3. DSC thermogram showing both the first heating (right-facing arrow) and cooling (left-facing arrow) cycles. The peaks marked with asterisks indicate exothermic peaks.

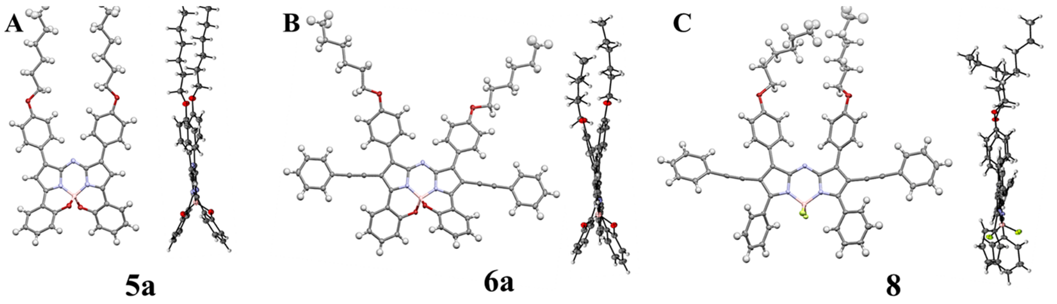

Figure 4. Ellipsoid plots of compounds **5a**, **6a**, and **8** (front and side views).

featureless heating profile for all complexes, further reinforcing the amorphous state of all of the complexes.

Geometric Characterization. Suitable crystals for single-crystal XRD were obtained from solvent diffusion in THF/MeOH, except for **6b**, which produced no resolvable crystals. Ellipsoid plots are shown in Figure 4. The side view shows that all of the boron complexes have a planar ADP core, including the phenylethynyl groups, and that the proximal phenyls of the BO complexes are more in-plane with the core than that of the BF_2 complex. To quantitatively characterize the structural features, we looked at the twisting angle of the phenyl rings out of the plane of the ADP core (α twisting angle) and the rotation angle of each phenyl ring with respect to the single bond connecting the phenyl ring to the ADP core (φ rotation angle), depicted in Figure 5 for the proximal phenyls. Specifically, the α twist angle is defined by the angle of the phenyl ring axis relative to the best-fit plane of the ADP core, and the φ rotation is defined as the dihedral angle between the plane of the phenyl ring and the best-fit plane of the ADP core. The measured angles for the proximal phenyls (pro), distal phenyls (dis), and pyrrolic phenyls (pyr) are collected in Table 1. The BO complexes tend to have smaller angles and thus are more planar than the BF_2 complex. To better understand the geometries of these complexes, we also computationally characterized all four compounds' lowest-lying ground-state geometries in the solvent phase with DFT. The computational structural characteristics are given in Table 1. The α angle and φ rotation of **5a** and **6a** are in agreement with both crystal structures and the solvent phase. This is because the BO complexes are geometrically constrained, leading to limited variation in the possible geometric configurations. Compound **8**, however, features fewer constraints because the proximal phenyls can freely rotate. The C−N−C (N is the bridging nitrogen to the pyrrole rings) angles can also affect planarization of the phenyls. The BO complexes in the crystal show $\sim$1° less than the solvent phase. This leads to better planarization of the distal phenyls, relieving steric effects, which then allow for the pyrrolic phenyls to also planarize.

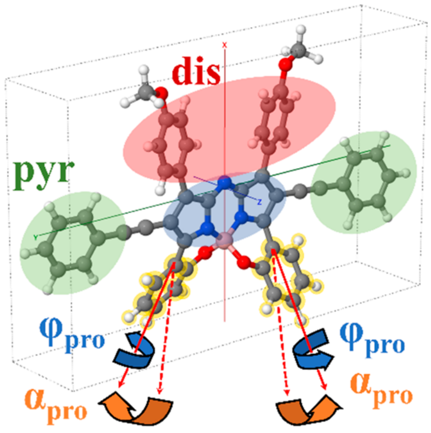

Figure 5. Measured α and φ angles of the proximal position. The α angle measures the degree to which the proximal phenyl ring twists out of the plane of the ADP core, while the φ angle is the dihedral angle between the plane of the proximal phenyl ring and the ADP core. Distal (dis) and pyrrolic (pyr) phenyls are highlighted in red and green, respectively.

Optical Properties. The optical properties are given in Figure 6 and summarized in Table 2. The UV−vis spectra in Figure 6a show that all complexes strongly absorb in the visible-to-NIR range. In solution, **5a** has a dark pink/purple color and has a strong and narrow absorption between 600 and 775 nm, with a maximum at 727 nm. Upon installing phenylethynyl groups (**6a**, dark blue in solution), this peak red-shifts to 781 nm, which we attribute to extension of the conjugation. When the intramolecular BO is replaced with BF_2 in **8** (blue-green in solution), the absorption spectra blue-shifts to 702 nm and significantly broadens. **6b** with intramolecular BO and phenylethynyls but no solubilizing groups is dark pink/purple in solutions and has a narrow peak at 791 nm, slightly red-shifted by 10 nm relative to **6a**. All BO complexes have a higher extinction coefficient than the BF_2 complex **8**. The lower extinction coefficient of the BF_2 complex **8** is most likely due to the increased conformational flexibility of **8**, which broadens the absorption and reduces the peak height.

Thin films were obtained by spin-coating from chloroform solutions. Compounds **5a**, **6a**, and **8** resulted in visually smooth films, while **6b** shows aggregation. The solubilizing groups are therefore important to obtain smooth and uniform films. λ_{max} values in the films in Figure 6b follow trends similar to those in solution. λ_{max} red-shifted from solution to film by 39−66 nm, consistent with $\pi-\pi$ stacking in films. Compounds with phenylethynyl groups had a much broader absorption band than **5a**, suggesting that these groups enhance $\pi-\pi$ stacking interactions in films. Interestingly, **6a**, which combines phenyethynyls at the pyrrolic positions and hexyloxy solubilizing groups, showed shoulders on each side of the main absorption peak, leading to the broadest peak and lowest optical gap of 1.22 eV. This indicates that the two types of substitutions combine to promote intermolecular interactions in films. Compound **6b** has a slightly higher optical gap of 1.26 eV, whereas **5a** and **8** have higher optical gaps of 1.50 and 1.52 eV, respectively. The films of **5a** and **6a** are optically clear, with relatively low absorption in the visible range. On the other hand, the BF_2 complex film has a slight blue-green color due to some absorption above 550 nm.

https://doi.org/10.1021/acs.inorgchem.1c01597
Inorg. Chem. XXXX, XXX, XXX−XXX

Table 1. Summarized Geometric Measurements from the Solvent Phase and Crystal Structure of the Four Compounds

		solvation (computational)			crystal (experimental)		
compound	position	α twist, deg	ϕ rotation, deg	C−N−C angle, deg	α twist, deg	ϕ rotation, deg	C−N−C angle, deg
5a	pro	26.2, 26.2	13.3, 13.5	119.1	30.6, 28.7	9.2, 12.1	117.73
	dis	1.5, 1.5	32.3, 32.3		2.8, 0.1	24.8, 30.5	
6a	pro	26.0, 26.0	14.0, 14.0	119.1	24.4, 24.4	14.2, 14.2	118.42
	dis	1.7, 1.7	39.6, 39.6		9.3, 9.3	10.6, 10.6	
	pyr	6.4, 6.5	14.3, 14.2		3.4, 3.4	1.3, 1.3	
8	pro	5.7, 5.7	56.4, 56.4	120.7	2.4, 11.4	56.3, 26.5	120.49
	dis	1.2, 1.2	44.9, 44.9		0.0, 0.1	33.6, 39.7	
	pyr	10.7, 10.7	5.5, 5.3		1.4, 5.6	29.5, 3.2	
6b	pro	26.3, 26.3	14.0, 14.0	119.0			
	dis	1.7, 1.7	42.3, 42.3				
	pyr	6.9, 6.9	14.4, 14.4				

The fluorescence spectra of chloroform solutions are shown in Figure 6c, and the emission properties are summarized in Table 3. All compounds showed fluorescence with a maximum in the NIR. Similar to trends observed in the absorption spectra, the emission maximum was the smallest for **5a**, at 741 nm, and red-shifts with phenylethynyl groups to 805 and 821 nm for **6a** and **6b**, respectively. Unlike in the absorption spectra, the BF_2 complex **8** has an emission at longer wavelength than **5a** despite having phenylethynyls. This is reflected in the large Stokes shift (SS) of 65 nm (or 1207 cm^{-1}) found for the BF_2 complex, compared to the very small SS of 13 nm (or 260 cm^{-1}) for **5a**. The fluorescence QYs varied from 1.0% for **8** to a high of 8.3% for **5a**. The QYs appear to inversely correlate with the observed SS: the lower the SS, the higher the QY. Compound **6a** shows good solubility in organic solvents, with a relatively high NIR QY of 6.0% at 805 nm.

Electrochemistry. Cyclic voltammograms of the complexes in dichloromethane (DCM) are shown in Figure 7, and the electrochemical properties are summarized in Table 4. All complexes show two reversible reduction processes and one irreversible oxidation process. Compound **5a** shows the anodic peak potential (E_{pa}) and first cathodic peak potential (E_{pc}) occurring at +0.56 and −1.01 V, respectively. Adding phenylethynyl (**6a**) increases E_{pa} to 0.70 V but does not significantly change the first E_{pc} (−0.98 V). Removing the intramolecular bonding in compound **8** increases both E_{pa} and E_{pc}. Removing the hexyloxy solubilizing groups (**6b**) increases the first E_{pc} compared to that of **6a**.

The ionization potential (IP) and EA were estimated from the onsets of the first reduction and oxidation waves and are reported in Table 4 and Figure 8a. The IP and EA for BF_2(WS3), the BF_2 analogue of **6b**, are also included for comparison. The negative values of the IP and EA are often used to approximate the highest occupied molecular orbital (HOMO) and lowest unoccupied molecular orbital (LUMO) energy levels, respectively.[29] The difference between the IP and EA is taken as the fundamental gap.[30] The results demonstrate that the IP and EA can be fine-tuned using with the chelation type and substitutions, with IP ranging from 5.26 eV for **5a** to 5.53 eV for **8** and EA ranging from 3.89 eV for **5a** to 4.15 eV for **6b**. The phenylethynyl pyrrolic groups increase both the IP and EA (or decrease the HOMO and LUMO energy levels). The intramolecular BO chelates decrease the IP and have very little effect on the EA [compare **6a** with **8** or **6b** with BF_2(WS3)]. This results in decreased fundamental gaps for the BO complexes. The hexyloxy solubilizing groups also slightly decrease the IP and EA [compare **6a** with **6b** and **8** with BF_2(WS3)].

Computation: Ground-State Properties. Vertical IPs and EAs were computed using the ΔSCF procedure (the energy difference between the relevant neutral and charged species of the ground-state geometry) and are summarized in Table S3. As shown in Figure 8a, the calculated IP and EA agree with the experimental values to within 0.24 eV. Generally, the calculated IPs are larger than the experimental values and the calculated EAs are smaller than the experiemental values, resulting in a larger calculated fundamental gap than the measured fundamental gap by 0.36−0.43 eV (Figure 8b). While the calculated and experimental values are different, the trends observed with the chemical structure are similar.

To gain direct insight into the electronic structure based on the above single-point-energy calculations, we look at the frontier orbitals. Figure 9 shows contour plots of the HOMO and LUMO for the four complexes. A considerable portion of the electron density of the frontier orbitals sits on the ADP core. This direct observation is supported by a Löwdin population analysis of the frontier molecular orbitals.[31] Table 5 shows the proportion of each frontier orbital contributed by the 12 atoms comprising the ADP core (Figure 5, highlighted in blue), as well as the net charge on the proximal phenyl rings. The ADP core contributes to 54−60% of the HOMO and 66−71% of the LUMO for all compounds. Interestingly, we find a linear relationship between the proximal charge and the IP, as shown in Figure 8c. This implies that greater electron density in the proximal phenyl rings reduces the IP.

Computation: Excited-State Properties. We simulated the optical absorption spectra using time-dependent DFT within the random-phase approximation. The resulting absorption spectra are shown in Figure 10. For all four molecules, the bright peak around 750 nm corresponds to the $S_0 \rightarrow S_1$ transition, which corresponds primarily to a HOMO → LUMO transition (>94% by weight). The energy and major transition components of the lowest four states are listed in Table S4. The computed oscillator strength for the lower-energy peak of the BF_2 complex **8** is 1.116, higher than that of the BO complex **6a** at 0.809. These results are consistent with our experimental results. BF_2 has a lower extinction coefficient than the BO complex because of the increased conformational flexibility, which broadens the absorption and reduces the peak height and, hence, the extinction coefficient. Taking this into account, the transition in **8** is actually stronger than the transition in the BO compounds. For instance, the full width at

https://doi.org/10.1021/acs.inorgchem.1c01597
Inorg. Chem. XXXX, XXX, XXX−XXX

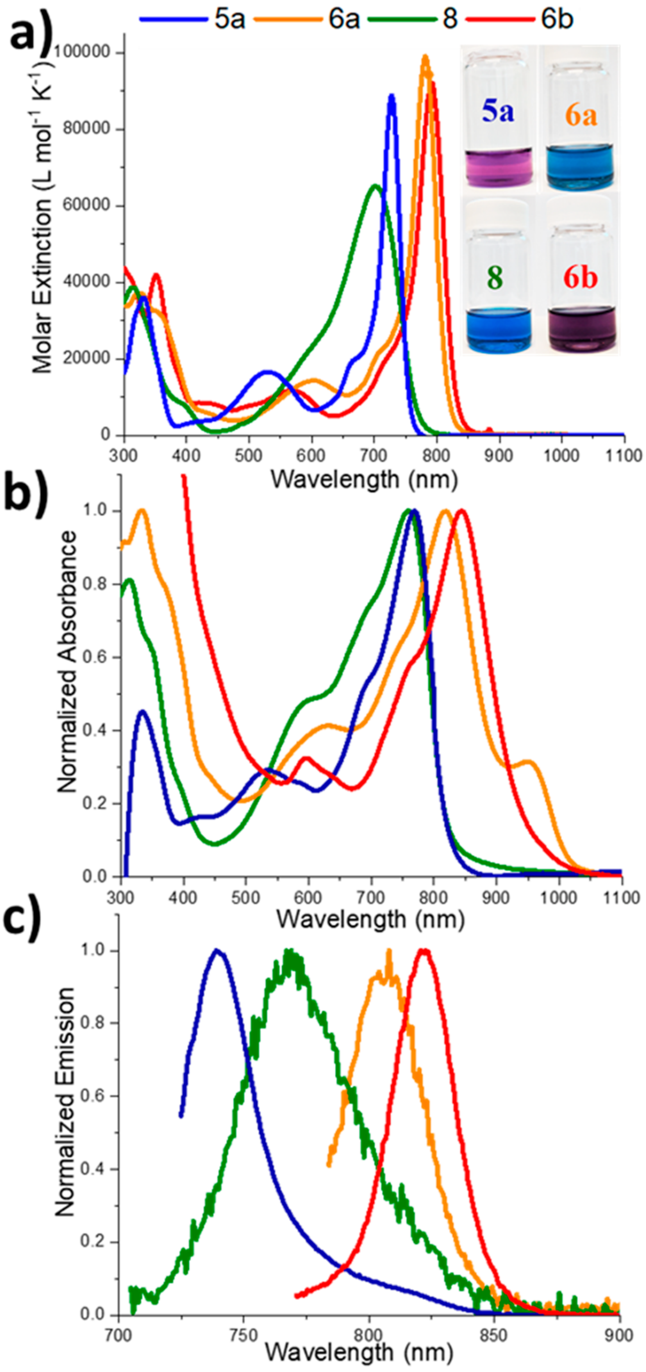

Figure 6. Optical properties of the compounds: (a) UV−vis spectra in $CHCl_3$ with solutions in the inset; (b) normalized UV−vis spectra of thin films spin-coated from $CHCl_3$; (c) normalized fluorescence spectra in $CHCl_3$.

Table 2. Summary of the Optical Properties

compound	$\lambda_{max,abs}$, nm (ε, L mol^{-1} cm^{-1})	λ_{max} film, nm	shift upon film formation, nm	λ_{onset}, nm	optical gap, eV
5a	331 (36000), 529 (17000), 727 (88000)	769	42	826	1.50
6a	325 (37000), 604 (14000), 781 (99000)	820	39	1010	1.22
8	315 (39000), 702 (65000)	761	59	818	1.52
6b	350 (42000), 569 (12000), 791 (92000)	857	66	984	1.26

Table 3. Summary of the Emission Properties[a]

compound	$\lambda_{max,em}$, nm	SS, nm	SS, cm^{-1}	Φ_{fluor}
5a	741	14	260	0.083
6a	805	24	382	0.060
8	767	65	1207	0.010
6b	821	30	462	0.043

[a] $\lambda_{max,em}$ is the maximum emission wavelength, SS is the Stokes shift, and Φ_{fluor} is the QY obtained using HITCI (Φ = 0.283 in ethanol) as the standard.

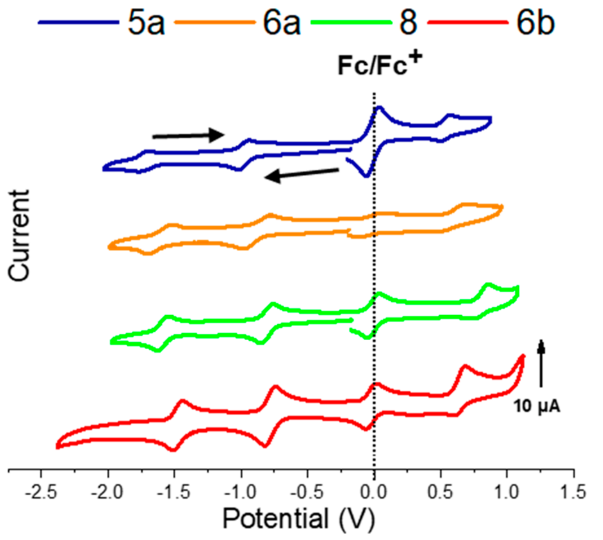

Figure 7. Cyclic voltammogram of compounds **1**−**4** with 0.1 M $TBAPF_6$ in DCM as an electrolyte solution. Fc/Fc$^+$ was used as the internal standard.

half-maximum (fwhm) of the lowest-energy absorption in **8** is 108 nm, compared to 43 nm for **6a**. The total transition strength is determined by integrating the extinction coefficient for a single peak, which is approximately proportional to the peak height times of the fwhm. Using this approach, we find that the total transition strength in **8** is 1.65 times stronger than the total transition strength in **6a**, which closely matches the ratio of the computed oscillator strength of 1.38.

We further performed natural transition orbital (NTO) analysis,[32] and the obtained contour plots are shown in Figure 11. For each compound, the S_1 transition is dominated by a single pair of transition orbitals with a singular value greater than 0.97. The NTO hole and electron orbitals strongly resemble the HOMO and LUMO, respectively, as expected for transitions dominated by a single HOMO-to-LUMO transition. Because the NTO pairs are both concentrated on the ADP core, we conclude that S_1 has an excitonic character with no significant intramolecular charge transfer.

■ CONCLUSIONS

In this study, we found that the optical, structural, and electrochemical properties can be tuned using hexyloxy solubilizing groups, pyrrolic phenylethynyls, and the boron coordination type. Hexyloxy groups on the distal phenyls increase the solubility in organic solvents, enable smooth

Table 4. Summary of the Electrochemical Properties from CV Using Fc/Fc$^+$ as the Internal Standard

compound	$E_{1/2\ ox}$, V	E_{pa}, V	$E_{1/2\ red}$, V	E_{pc}, V	$E_{ox\ onset}$, V	$E_{red\ onset}$, V	IP, eV	EA, eV	E_{gap},[a] eV
5a		0.56	−0.97, −1.73	−1.01, −1.77	0.46	−0.91	5.26	3.89	1.37
6a		0.70	−0.88, −1.61	−0.98, −1.69	0.54	−0.76	5.34	4.04	1.30
8		0.86	−0.80, −1.59	−0.84, −1.63	0.73	−0.77	5.53	4.06	1.47
6b		0.68	−0.78, −1.47	−0.82, −1.51	0.61	−0.65	5.41	4.15	1.26
BF_2(WS3)[b]		1.08	−0.79, −1.59	−0.95, −1.75	0.86	−0.70	5.66	4.10	1.56

[a] E_{gap} is the fundamental gap. [b] Electrochemical properties reproduced from ref 19.

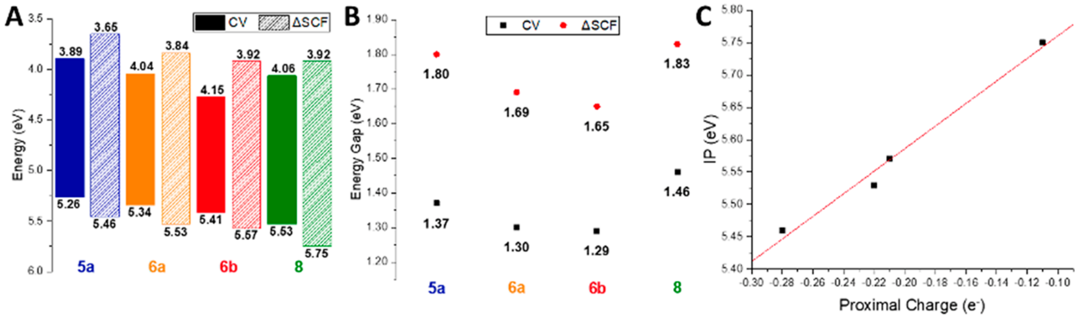

Figure 8. (a) Estimated energy levels of the complexes in solution, taking $E_{1/2}$ of Fc/Fc$^+$ as −4.8 eV versus vacuum with energy levels from ΔSCF calculation, (b) fundamental gaps obtained from CV and ΔSCF calculations, and (c) computed IP versus computed proximal phenyl charge.

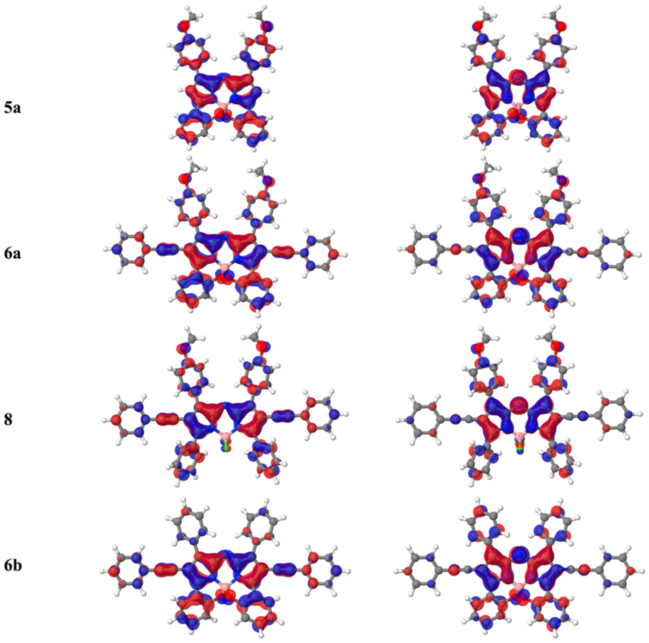

Figure 9. Contour plots of the HOMO (left) and LUMO (right), plotted with an isovalue of 0.02 Å^{-3}.

Table 5. ADP Core Percentage Contributions (%) to the Molecular Orbital, Löwdin Atomic Charges of the ADP Core, and Simulated IPs

compound	HOMO	LUMO	proximal charge, e$^-$	IP, eV
5a	60	68	−0.28	5.46
6a	54	7	−0.22	5.53
8	58	72	−0.11	5.75
6b	55	68	−0.21	5.57

solution-processed films, facilitate crystallization, slightly blue-shift the absorption and emission peaks, and slightly lower the IP and EA. The pyrrolic phenylethynyls extend the conjugation of the ADP core to red-shift the absorption and emission spectra and increase the IP and EA. Intramolecular BO complexation constrains the proximal phenyl rotation, resulting in smaller rotation angles and thus planarization of the conjugated molecule. DFT calculations show that BO complexation also leads to better planarization of the distal phenyls and relieves steric effects, which then allows for the pyrrolic phenyls to also planarize. This significantly red-shifts the absorption and emission spectra, resulting in smaller optical gaps. The BO complexes tend to have smaller SSs and larger fluorescence QYs than the BF_2 complex. The $S_0 \rightarrow S_1$ excitation was found to correspond to a HOMO-to-LUMO transition with no significant intramolecular charge-transfer character. For ADP functionalized with both hexyloxy and phenylethynyl groups, the BO complex (**6a**) has NIR optical properties with λ_{max} of 781 nm in solution, an emission at 805 nm, and a QY of 6%. It forms films that look transparent with a low optical gap of 1.22 eV. This makes **6a** promising for transparent organic solar cells and NIR photodetectors. Changing the boron coordination to BF_2 increases the optical gap to 1.52 eV, mainly because of an increase in the IP. DFT calculations showed that the electron density on the proximal phenyls directly correlates with the new complex's IP. This work advances the development of NIR chromophores and extends the application of ADP-based dyes.

■ EXPERIMENTAL SECTION

Characterization. ^{1}H, ^{19}F, ^{11}B, and ^{13}C NMR spectra were recorded using a 500 MHz Bruker Ascend Advance III HDTM spectrometer equipped with a Prodigy ultrahigh-sensitivity Multinuclear Broadband CryoProbe. Glassware was precleaned and flame-dried prior to use. MALDI-TOF mass spectrometry spectra were acquired in reflective negative mode on a Bruker Autoflex III Smartbeam MALDI-TOF spectrometer with terthiophene as the matrix. Elemental analysis was performed by Robertson Microlit Laboratories.

Thermal Measurements. Thermal measurements were conducted with DSC measurements and taken with a DSC Q100 series from TA Instruments with a ramp rate of 10 °C/min. Samples were analyzed as crystalline solids. All samples were hermetically sealed

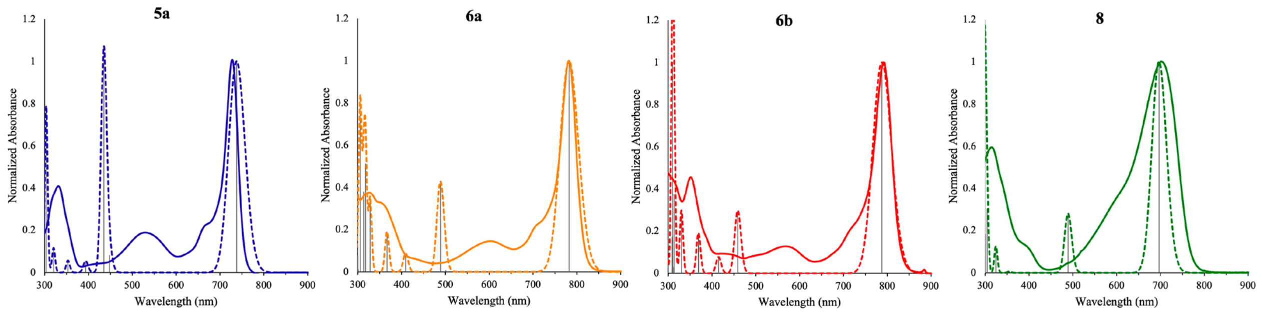

Figure 10. Simulated UV−vis spectra (dashed) compared to measured spectra (solid). Simulated spectra are broadened by a Gaussian with a fwhm of 0.1 eV and uniformly shifted by −0.40 eV.

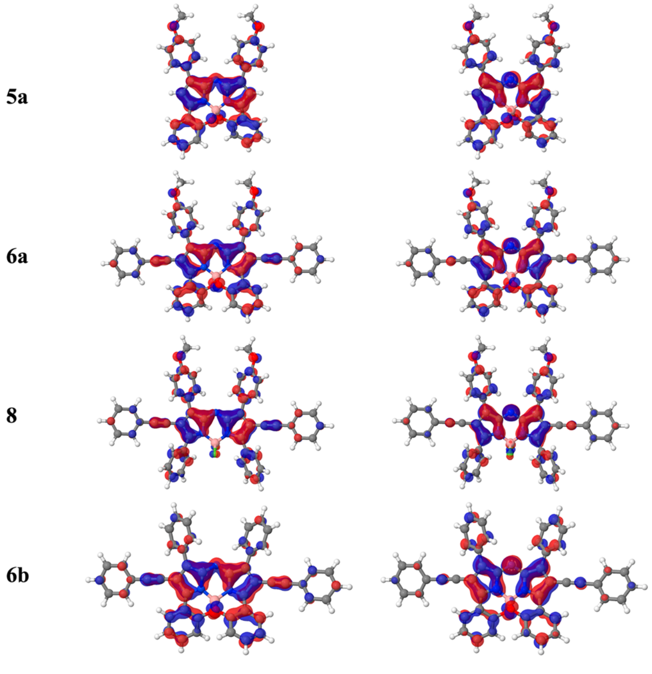

Figure 11. NTO hole and electron orbitals for the $S_0 \rightarrow S_1$ excitation of four compounds ($S_0 \rightarrow S_1$ singular values are 0.974, 0.974, 0.977, and 0.975 for compounds **5a**, **6a**, **8**, and **6b**, respectively), plotted with isovalue = 0.02 Å^{-3}.

using aluminum pans, and a hermetically sealed blank aluminum pan was used as the reference. TGA was performed using a Q500 series with a ramp rate of 10 °C/min. The substrate was a platinum pan that was incinerated with a butane torch prior to use. Both T_m and T_{d5} (temperature at 5% weight loss) were determined from thermal measurements.

Optical Properties. Film and solution UV−vis measurements were collected on a Cary 5000 UV−vis−NIR spectrophotometer with high-performance liquid chromatography (HPLC)-grade chloroform in a quart cuvette. Solutions were made from 1 mg of material with 1 mL of HPLC-grade chloroform. Thin films of the compounds were prepared using a 2 mg/mL solution in $CHCl_3$, which was stirred at 50 °C overnight. Solutions were casted onto cleaned borosilicate glass using a syringe and passed through a 0.22 μm poly(tetrafluoroethylene) filter. The glass substrates were spin-coated with a Laurell WS-650 spin coater at 2000 rpm for 30 s. Fluorescence measurements were obtained on a Cary Eclipse fluorimeter using quartz cuvettes with a Teflon cap. Solutions were obtained from a 1 mg/mL stock solution and then diluted so that the absorbance values were below 0.1 to minimize inner-filter effects. QYs were obtained using 97% 1,1′,3,3,3′,3′-hexamethylindotricarbocyanine iodide (HITCI) as the standard (st) because λ_{abs} is 743 nm and λ_{em} is 772 nm, suitable for our complexes (Φ_F = 0.283 in ethanol).[33,34] All compounds were dissolved with HPLC-grade solvent, and measurements were taken without any inert gas sparging. Equation 1 was used to calculate the QYs:[35]

$$\Phi F_{sample} = \Phi F_{st} \frac{\text{Slope}_{sample}}{\text{Slope}_{st}} \frac{{\eta_{sample}}^2}{{\eta_{st}}^2} \tag{1}$$

where Slope$_{st}$ is the slope of a graph of integrated fluorescence intensity versus absorbance plot for the standard (HITCI), Slope$_{sample}$ is the slope of a graph of integrated fluorescence intensity versus absorbance plot for the sample, η_{st} is the refractive index of the solvent used for the standard (here, ethanol, 1.36), and η_{sample} is the refractive index of the solvent used for the sample (here, chloroform, 1.45).

Electrochemistry. Cyclic voltammetry measurements were obtained using an Eco Chemie AutoLab PGSTAT302N potentiostat at room temperature at a scan rate of 0.1 V/s. Glassware was thoroughly cleaned and dried in the oven overnight prior to use. Extra-dry DCM obtained from Acros Organics was the solvent. Ferrocene was purified via sublimation, and tetra-*n*-butylammonium-hexafluorophosphate ($TBAPF_6$) was recrystallized from MeOH, which was then used to make the supporting electrolyte (0.1 M). The three-electrode configuration used a freshly polished glassy carbon electrode as the working electrode, a platinum electrode as the counter electrode, and a freshly polished glassy carbon electrode as the reference electrode. The IP and EA were determined by extrapolation of the onsets for the first oxidation and reduction events, using the value of −4.8 eV for Fc/Fc$^+$. The estimated energy levels were calculated using

$$E_{IP} = E_{onset}(\text{Ox}) + 4.8\ \text{eV}$$

$$E_{EA} = E_{onset}(\text{Red}) + 4.8\ \text{eV}$$

where E_{onset}(Ox) is the onset of the first oxidation, E_{onset}(Red) is the onset of the first reduction, and 4.8 eV is the electrochemical half-potential of Fc/Fc$^+$.

Crystallography. Suitable crystals of all compounds were obtained from solvent diffusion from THF and MeOH as the antisolvent. Care was taken that the carefully layered solvents were not disturbed; otherwise, the crystals would degrade. Data were collected at 100 K using either Cu or Mo rotating anode sources on Bruker diffractometers equipped with microfocus optics. In most cases, high-resolution data were not available because of very weak diffraction at high 2*θ* values. Nonetheless, data provided unambiguous structural characterizations despite the frequent presence of slightly-to-highly disordered alkyl chains.

Geometry Optimization. First, all of the hexyloxy groups were replaced with methoxy groups to streamline the calculations. Then we used the Conformer-Rotamer Ensemble Sampling Tool (xtb-CREST) with the GFN2 force field to generate low-lying conformers.[36−38] Next, all conformers were optimized using DFT. We applied tight self-consistent-field (SCF) convergence thresholds ("TightSCF" option, grid 4, final grid 6), with the TPSS density functional with D3 dispersion corrections using the Becke−Johnson damping scheme [D3(BJ)] and the def2-TZVP basis set.[39−42] In all cases, the resolution of the identity was used to approximate the Coulomb integrals in combination with the def2/J auxiliary basis set.[43,44] Solvation effects were included with the conductor-like polarizable continuum model (CPCM) using dielectric constant 8.93 (DCM).[45] For each molecule, the conformer with the lowest TPSS energy was finally optimized with ωB97X-D3BJ/def2-TZVP/CPCM with exchange-type two-electron integrals approximated using the chain of spheres (COSX) with GRIDX8 and using "TightSCF" and "TightOpt" as the SCF and geometry optimization criteria, respectively.[46−48] All results reported use these optimized structures. All other conformers found to be within 1 kcal/mol (by TPSS) of the lowest-energy conformer are presented in the Supporting Information. For all calculations, we used *ORCA 4.2*.[49]

Single-Point Calculation. The SCF energies of the neutral species, cations, and anions were computed using ωB97X-D3BJ/def2-TZVP/CPCM as described above.

Absorption Spectrum. For each spectrum, we computed the 15 lowest singlet excited states with ωB97X-D3BJ/def2-TZVP/CPCM and broadened the stick spectrum using Gaussians with a fwhm of 0.1 eV. A uniform shift of −0.40 eV was applied to all simulated spectra to assist in visual comparison.

NTO Analysis. We use *TheoDORE* to perform NTO analysis.[50] The NTO pair with the largest singular value for the bright S_1 state is shown in Figure 11, along with the associated singular value.

Synthesis. *4-Hexyloxybenzaldehyde (**1a**).* The synthesis was done according to the literature.[51] The compound was used directly in the next step.

*2′-Hydroxy-4-hexyloxychalcone (**3a**).* 2′-Hydroxyacetophenone (**2a**; 5.65 g, 27.39 mmol), **1a** (3.73 g, 27.39 mmol), and sodium hydroxide (3.29 g, 82.17 mmol) were added to a mortar and ground using a pestle until an orange paste formed. The paste was left to dry for 1 h and then ground into a fine orange powder. The powder was dissolved in MeOH and then neutralized with 1 M HCl to precipitate bright-yellow solids. The solids were filtered and then recrystallized in MeOH as bright-yellow crystals (4.13 g, 12.7 mmol, 46.5% yield). ^{1}H NMR (500 MHz, chloroform-*d*): δ 12.95 (s, 1H), 7.96−7.88 (m, 2H), 7.65−7.59 (m, 2H), 7.54 (d, J = 15.4 Hz, 1H), 7.49 (td, J = 7.9 and 1.6 Hz, 1H), 7.02 (d, J = 8.4 Hz, 1H), 6.94 (dd, J = 8.0 and 5.7 Hz, 3H), 4.02 (t, J = 6.6 Hz, 2H), 1.85−1.76 (m, 2H), 1.60−1.41 (m, 2H), 1.41−1.30 (m, 4H), 0.91 (t, 3H). ^{13}C NMR (126 MHz, $CDCl_3$): δ 193.84, 163.70, 161.84, 145.64, 136.26, 130.72, 129.67, 127.25, 120.29, 118.89, 118.74, 117.54, 115.15, 77.41, 77.36, 77.16, 76.91, 68.41, 31.71, 29.26, 25.83, 22.75, 14.19.

*4-Hexyloxychalcone (**3b**).* 4-Hexyloxybenzaldehyde[1] (**1b**; 1.75 g, 14.54 mmol), acetophenone (**2b**; 3.00 g, 14.54 mmol), and sodium hydroxide (640 mg, 16.00 mmol) were added to a mortar and ground using a pestle until an off-white paste formed. The paste was left to dry for 1 h and then further ground to a powder. The powder was recrystallized from MeOH and then filtered as an off-white solid (4.49 g, 14.5 mmol, 64.4% yield). ^{1}H NMR (500 MHz, chloroform-*d*): δ 8.01 (dt, J = 7.1 and 1.4 Hz, 2H), 7.79 (d, J = 15.6 Hz, 1H), 7.60 (s, 1H), 7.59−7.54 (m, 2H), 7.50 (dd, J = 8.3 and 6.9 Hz, 2H), 7.41 (d, J = 15.6 Hz, 1H), 6.95−6.90 (m, 2H), 4.00 (t, J = 6.6 Hz, 2H), 1.80 (p, J = 6.7 Hz, 2H), 1.47 (p, 2H), 1.40−1.30 (m, 4H), 0.91 (t, 3H). ^{13}C NMR (126 MHz, $CDCl_3$): δ 190.77, 161.48, 144.98, 138.70, 132.66, 130.38, 128.70, 128.56, 128.45, 127.51, 119.75, 115.06, 77.41, 77.16, 76.91, 68.35, 31.71, 29.27, 25.83, 22.75, 14.18.

*(Z)-2-[3-[4-(Hexyloxy)phenyl]]-2-[[3-[4-(hexyloxy)phenyl]-5-(2-hydroxyphenyl)-1H-pyrrol-2-yl]imino]-2H-pyrrol-5-yl]phenol (**4a**).* **3a** (4.00 g, 12.33 mmol), nitromethane (3.76 g, 61.65 mmol), and triethylamime (5.24 g, 61.65 mmol) were added into a 200 mL Schlenk flask with 100 mL of MeOH and then refluxed for 16 h. The solution was cooled in an ice bath and then neutralized with 1 M HCl until pH ∼2 and precipitates formed. The solids were filtered and then dried under vacuum. The solids were added to a 200 mL round-bottom flask with 100 mL of 1-BuOH and ammonium acetate (33.25 g, 431.30 mmol) and then refluxed for 16 h. The solution was a heterogeneous mixture of a dark-blue-green solution with red precipitates. The solids were filtered into a Hirsch funnel and then washed with MeOH until the filtrate was clear and then with hexanes. The resulting product is a red metallic solid (1.52 g, 2.23 mmol, 36.2% yield). MALDI-TOF: m/z 681.31. Calcd: m/z 681.36. ^{1}H NMR (500 MHz, chloroform-*d*): δ 7.91−7.85 (m, 4H), 7.70 (d, J = 7.8 Hz, 2H), 7.19 (t, J = 7.6 Hz, 2H), 7.13 (s, 2H), 7.00 (d, J = 8.3 Hz, 2H), 6.96−6.87 (m, 6H), 4.03 (t, J = 6.6 Hz, 4H), 1.85 (p, J = 6.8 Hz, 4H), 1.51 (p, J = 6.8 Hz, 4H), 1.41−1.35 (m, 8H), 0.94 (t, J = 6.9 Hz, 6H). ^{13}C NMR (126 MHz, $CDCl_3$): δ 159.88, 157.33, 154.45, 142.42, 131.94, 131.27, 128.65, 126.54, 120.88, 117.63, 117.14, 114.68, 113.82, 77.67, 77.41, 77.16, 68.52, 32.06, 29.72, 26.21, 23.05, 14.48.

*6,8-Bis[4-(hexyloxy)phenyl]-14,15-dioxa-4b1,7,7a114-triaza-14a14-borabenzo[6,7]indeno[3,4-ef]aceanthrylene (**5a**; CCDC 2084913).* In a 50 mL Schlenk flask attached to a reflux condenser, **4a** (1.00 g, 1.47 mmol) was added and then purged with nitrogen three times. Dry toluene (25 mL) and then BF_3OEt_2 (2.08 g, 14.67 mmol) were added via a syringe and then stirred for 30 min at reflux. Dry diisopropylethylamine (3.79 g, 29.33 mmol) was added via a syringe and then stirred for an additional 3 h. The solution was cooled to room temperature and then evaporated via a rotary evaporator until dry. The solids were recrystallized from vapor diffusion using THF/pentanes. Red metallic crystals were obtained that were washed with MeOH and then dried. The resulting solid was a metallic red solid (0.75 g, 1.09 mmol, 74.2% yield). MALDI-TOF: m/z 689.427. Calcd: m/z 689.66. ^{1}H NMR (500 MHz, chloroform-*d*): δ 8.16−8.09 (m, 4H), 7.84 (dd, J = 7.6 and 1.6 Hz, 2H), 7.39 (ddd, J = 8.6, 7.2, and 1.7 Hz, 2H), 7.12 (s, 2H), 7.10 (td, J = 7.5 and 1.1 Hz, 2H), 7.03−6.97 (m, 6H), 4.05 (t, J = 6.7 Hz, 4H), 1.84 (p, J = 6.7 Hz, 4H), 1.51 (p, J = 7.2 Hz, 4H), 1.43−1.34 (m, 8H), 0.93 (t, J = 7.0 Hz, 6H). ^{13}C NMR (126 MHz, $CDCl_3$): δ 160.55, 156.19, 149.73, 144.83, 142.20, 133.20, 130.67, 126.70, 125.26, 120.95, 120.33, 119.16, 114.96, 111.57, 77.41, 77.36, 77.16, 76.91, 68.34, 31.76, 29.38, 25.89, 22.78, 14.21. ^{11}B NMR (160 MHz, $CDCl_3$): δ −1.60. Elem anal. Found: C, 76.56; H, 6.39; N, 6.21. Calcd: C, 76.63; H, 6.43; N, 6.09. T_m = 236 °C; T_{d5} = 390 °C.

*6,8-Bis[4-(hexyloxy)phenyl]-5,9-bis(phenylethynyl)-14,15-dioxa-4b1,7,7a1-triaza-14a14-borabenzo[6,7]indeno[3,4-ef]-aceanthrylen-7a1-ium (**6a**; CCDC 2084912).* **4a** (750 mg, 1.09 mmol) and *N*-iodosuccinimide (562 mg, 2.50 mmol) were used, resulting in a solid (630 mg, 0.890 mmol, 61.5% yield), of which 300 mg was directly used in the next step. In the second step, tributyl(phenylethynyl)stannane (374 mg, 0.956 mmol) and $Pd(PPh_3)_4$ (37 mg, 0.032 mmol) were added in the same manner as that of the previous compound. The solution turned from purple/pink to dark cyan in color. The resulting solids were recrystallized in THF/MeOH via solvent diffusion. The crystals were filtered and dried under vacuum, resulting as a shiny, metallic blue-green solid (176 mg, 0.198 mmol, 62.1% yield). MALDI-TOF: m/z 889.638. Calcd: m/z 889.40. ^{1}H NMR (500 MHz, chloroform-*d*): δ 8.68 (d, J = 8.1 Hz, 2H), 8.41−8.36 (m, 4H), 7.63−7.57 (m, 4H), 7.43 (dt, J = 14.9 and 8.1 Hz, 8H), 7.18 (t, J = 7.5 Hz, 2H), 7.06−7.01 (m, 6H), 4.07 (t, J = 6.6 Hz, 4H), 1.85 (p, J = 6.9 Hz, 4H), 1.55 (s, 21H), 1.51 (p, J = 7.9 and 7.5 Hz, 3H), 1.38 (h, J = 3.8 Hz, 8H), 0.93 (t, J = 6.9 Hz, 6H). ^{13}C NMR (126 MHz, $CDCl_3$): δ 160.67, 156.30, 149.87, 144.43, 141.54, 133.95, 132.01, 131.43, 128.77, 128.74, 127.99, 124.62, 123.45, 120.97, 120.13, 119.18, 114.56, 108.85, 98.56, 84.42, 68.33, 31.76, 29.39, 25.90, 22.78, 14.21. ^{11}B NMR (160 MHz, $CDCl_3$): δ −1.64. Elem anal. Found: C, 80.93; H, 5.85; N, 4.59. Calcd: C, 80.98; H, 5.89; N, 4.72. T_m = 290 °C; T_{d5} = 400 °C.

*6,8-Diphenyl-5,9-bis(phenylethynyl)-14,15-dioxa-4b1,7,7a1-triaza-14a14-borabenzo[6,7]indeno[3,4-ef]aceanthrylen-7a1-ium (**6b**).* **4b** and **5b** were made according to the literature.[17] **5b** (482 mg, 0.650 mmol), tributyl(phenylethynyl)stannane (763 mg, 1.95 mmol), and $Pd(PPh_3)_4$ (46 mg, 0.065 mmol) were added into a 200 mL Schlenk flask. Once evaporated, the dried solids were washed with MeOH and then redissolved in DCM, and ethyl acetate was then added. The compound was precipitated from removal of DCM and then filtered. The product was recrystallized from $CHCl_3$/MeOH via solvent diffusion as a metallic blue-green solid (336 mg, 0.487 mmol, 74.9% yield). MALDI-TOF: m/z 689.411. Calcd: m/z 689.23. ^{1}H NMR (500 MHz, chloroform-*d*): δ 8.70 (dd, J = 8.0 and 1.7 Hz, 2H), 8.41−8.29 (m, 4H), 7.64−7.55 (m, 4H), 7.54−7.45 (m, 8H), 7.44−7.37 (m, 6H), 7.23−7.16 (m, 2H), 7.05 (dd, J = 8.3 and 1.1 Hz, 2H). ^{13}C NMR (126 MHz, $CDCl_3$): δ 156.14, 150.02, 144.72, 141.74, 134.31, 131.79, 131.51, 130.43, 129.64, 128.96, 128.77, 128.47, 128.03, 123.24, 121.16, 120.19, 119.07, 110.77, 99.10, 83.96. ^{11}B NMR (160 MHz, $CDCl_3$): δ −1.61. Elem anal. Found: C, 82.96; H, 3.49; N, 6.04. Calcd: C, 83.61; H, 4.09; N, 6.09. T_{d5} = 522 °C.

*(Z)-3-[4-(Hexyloxy)phenyl]-N-[3-[4-(hexyloxy)phenyl]-5-phenyl-1H-pyrrol-2-yl]-5-phenyl-2H-pyrrol-2-imine (**4c**).* The procedure is similar to the synthesis of **4a**. **3b** (2.50 g, 8.11 mmol), nitromethane (2.47 g, 40.53 mmol), and trimethylamine (4.10 g, 40.53 mmol) were added then in the next step with ammonium acetate (10.94 g, 141.92 mmol). The solution was refluxed for 16 h. The resulting reaction produced a heterogeneous mixture of dark blue/purple solution with a metallic yellow precipitate. The solution was evaporated with a rotary evaporator into a dry solid. The solid was resuspended in MeOH, which was filtered and then washed with MeOH and then with hexanes. The resulting solid was dried under vacuum as a metallic yellow/blue solid (0.55 g, 846 mmol, 41.7% yield). MALDI-TOF: m/z 649.247. Calcd: m/z 649.37. ^{1}H NMR (500 MHz, chloroform-d): δ 12.74 (s, 1H), 8.06−7.99 (m, 4H), 7.97−7.92 (m, 4H), 7.53 (t, J = 7.6 Hz, 4H), 7.45 (t, J = 7.3 Hz, 2H), 7.11 (s, 2H), 7.00−6.93 (m, 4H), 4.04 (t, J = 6.6 Hz, 4H), 1.84 (p, J = 6.8 Hz, 4H), 1.51 (p, J = 7.3 Hz, 4H), 1.38 (p, J = 6.8 and 4.4 Hz, 8H), 0.93 (t, J = 6.9 Hz, 6H). ^{13}C NMR (126 MHz, $CDCl_3$): δ 159.45, 155.04, 149.66, 142.53, 132.51, 130.49, 130.01, 129.22, 126.63, 114.50, 113.57, 77.41, 77.36, 77.16, 76.91, 68.27, 31.79, 29.44, 25.93, 22.79, 14.22.

*(Z)-3-[4-(Hexyloxy)phenyl]-N-[3-[4-(hexyloxy)phenyl]-5-phenyl-4-(phenylethynyl)-1H-pyrrol-2-yl]-5-phenyl-4-(phenylethynyl)-2H-pyrrol-2-imine (**7**).* **4a** (1.00 g, 1.54 mmol) and N-iodosuccinimide (727 mg, 3.23 mmol) were added to a 100 mL Schlenk flask with 50 mL of degassed chloroform and 2 drops of glacial acetic acid. The solution was stirred for 16 h, evaporated via a rotary evaporator, resuspended in MeOH, and then filtered. The solids were then dried under vacuum and used directly. Solids (500 mg) were added to a 100 mL Schlenk flask and then purged three times with nitrogen. The flask was transferred into a glovebox, where $Pd(PPh_3)_4$ (64 mg, 0.055 mmol) was added. The flask was taken out of the glovebox and then charged with 50 mL of dry xylenes and tributyl(phenylethynyl)-stannane (651 mg, 1.66 mmol) of via a syringe. The solution was heated to 135 °C for 16 h; meanwhile, the color went from dark purple to dark blue. The resulting solution was evaporated via a rotary evaporator, then resuspended in MeOH, filtered, and then washed with hot ethyl acetate until no color persisted in the washes. The solid was dried under vacuum, resulting in a metallic purple/red solid. The solid was confirmed by NMR, with the molecular mass of the solids confirmed by MALDI-TOF (345 mg, 0.406 mmol, 73.2% yield). MALDI-TOF: m/z 849.507. Calcd: m/z 849.43. ^{1}H NMR (500 MHz, chloroform-d): δ 12.69 (s, 1H), 8.29−8.21 (m, 4H), 8.17 (d, J = 8.6 Hz, 4H), 7.55−7.40 (m, 10H), 7.38−7.28 (m, 6H), 6.93 (d, J = 8.6 Hz, 4H), 4.05 (t, J = 6.6 Hz, 4H), 1.93−1.78 (m, 4H), 1.53 (p, J = 7.0 Hz, 4H), 1.46−1.36 (m, 8H), 1.00−0.91 (m, 6H). ^{13}C NMR (126 MHz, $CDCl_3$): δ 159.62, 155.57, 149.09, 142.94, 132.42, 132.06, 131.22, 130.24, 128.84, 128.54, 128.22, 125.54, 123.97, 113.95, 110.16, 97.73, 86.17, 77.41, 77.16, 76.91, 68.21, 31.83, 29.49, 25.97, 22.82, 14.24.

*5,5-Difluoro-1,9-bis[4-(hexyloxy)phenyl]-3,7-diphenyl-2,8-bis-(phenylethynyl)-5H-5l4-dipyrrolo[1,2-c:2′,1′-f][1,3,5,2]-triazaborinin-4-ium (**8**; CCDC 2084914).* **4b** (50 mg, 0.059 mmol) was added to a 100 mL Schlenk flask with 50 mL of dry toluene for 30 min under reflux conditions. BF_3OEt_2 (84 mg, 0.59 mmol) and diisopropylethylamine (78 mg, 0.588 mmol) were added dropwise, then stirred for 3 h, and then cooled to room temperature. The solution was washed with three aliquots of water (10 mL), then dried with magnesium sulfate, and then passed through a plug of Celite. The compound was evaporated and then recrystallized in DCM and MeOH. The solids were dried under vacuum, resulting in crystalline metallic purple solids (45 mg, 0.050 mmol, 85% yield). MALDI-TOF: m/z 897.650. Calcd: m/z 897.43. ^{1}H NMR (500 MHz, chloroform-d): δ 8.35−8.29 (m, 4H), 8.02 (dd, J = 6.6 and 2.9 Hz, 4H), 7.55−7.42 (m, 6H), 7.35−7.26 (m, 10H), 7.06−6.99 (m, 4H), 4.09 (t, J = 6.6 Hz, 4H), 1.86 (p, J = 6.8 Hz, 4H), 1.52 (p, J = 7.2 and 6.5 Hz, 4H), 1.44−1.34 (m, 8H), 0.94 (t, J = 6.6 Hz, 6H). ^{13}C NMR (126 MHz, $CDCl_3$): δ 161.56, 160.94, 144.68, 143.23, 132.38, 131.25, 130.96, 130.57, 130.31, 128.52, 128.49, 127.96, 124.64, 123.39, 114.46, 97.27, 84.16, 68.38, 31.77, 29.38, 25.92, 22.79, 14.22. ^{11}B NMR (160 MHz, $CDCl_3$): δ 0.71, 0.52, 0.34. ^{19}F NMR (471 MHz, $CDCl_3$): δ −130.69, −130.76, −130.83, −130.89. Elem anal. Found: C, 80.45; H, 6.27; N, 4.86. Calcd: C, 80.26; H, 6.06; N, 4.68. T_m = 230 °C; T_{d5} = 413 °C.

■ ASSOCIATED CONTENT

Supporting Information

The Supporting Information is available free of charge at https://pubs.acs.org/doi/10.1021/acs.inorgchem.1c01597.

> TGA thermograms, DSC thermograms of the second heat cycle, a summary of the thermal properties, MALDI-TOF spectra of all new compounds, computational details including conformers' geometry, ground- and excited-state properties, and ^{1}H and ^{13}C NMR spectra of all new compounds (PDF)

Accession Codes

CCDC 2084912−2084914 contain the supplementary crystallographic data for this paper. These data can be obtained free of charge via www.ccdc.cam.ac.uk/data_request/cif, or by emailing data_request@ccdc.cam.ac.uk, or by contacting The Cambridge Crystallographic Data Centre, 12 Union Road, Cambridge CB2 1EZ, UK; fax: +44 1223 336033.

■ AUTHOR INFORMATION

Corresponding Author

Geneviève Sauvé − *Department of Chemistry, Case Western Reserve University, Cleveland, Ohio 44106, United States;* orcid.org/0000-0002-9721-0447;
Email: genevieve.sauve@case.edu

Authors

Jayvic C. Jimenez − *Department of Chemistry, Case Western Reserve University, Cleveland, Ohio 44106, United States;* orcid.org/0000-0002-2342-5648

Zehao Zhou − *Department of Chemistry, Case Western Reserve University, Cleveland, Ohio 44106, United States;* orcid.org/0000-0003-2185-6855

Arnold L. Rheingold − *Department of Chemistry and Biochemistry, University of California, San Diego, La Jolla, California 92093, United States;* orcid.org/0000-0003-4472-8127

Shane M. Parker − *Department of Chemistry, Case Western Reserve University, Cleveland, Ohio 44106, United States;* orcid.org/0000-0002-1110-3393

Complete contact information is available at:
https://pubs.acs.org/10.1021/acs.inorgchem.1c01597

Author Contributions

The manuscript was written through contributions of all authors. All authors have given approval to the final version of the manuscript.

Notes

The authors declare no competing financial interest.

■ ACKNOWLEDGMENTS

We are thankful for the National Science Foundation (NSF; Grant CHEM 19048678) for funding the experimental part of this work and Case Western Reserve University for funding the computational part of this work. The authors thank Yibin Mao (CWRU) and Adam Wade (Hillsdale College) for their help in the synthesis and Dr. John D. Protasiewicz for access to cyclic voltammetry instrumentation. This project was possible thanks to Grant NSF MRI-0821515 for MALDI-TOF instrumentation and Grant NSF MRI-1334048 for NMR instrumentation. This work made use of the High Performance Computing Resource in the Core Facility for Advanced Research Computing at Case Western Reserve University.

REFERENCES

(1) Chen, C.; Tian, R.; Zeng, Y.; Chu, C.; Liu, G. Activatable fluorescence probes for "turn-on" and ratiometric biosensing and bioimaging: From NIR-I to NIR-II. *Bioconjugate Chem.* **2020**, *31* (2), 276−292.

(2) Luo, S.; Zhang, E.; Su, Y.; Cheng, T.; Shi, C. A review of NIR dyes in cancer targeting and imaging. *Biomaterials* **2011**, *32* (29), 7127−7138.

(3) Ni, Y.; Wu, J. Far-red and near infrared BODIPY dyes: synthesis and applications for fluorescent pH probes and bio-imaging. *Org. Biomol. Chem.* **2014**, *12* (23), 3774−3791.

(4) Lee, C.-P.; Lin, R. Y.-Y.; Lin, L.-Y.; Li, C.-T.; Chu, T.-C.; Sun, S.-S.; Lin, J. T.; Ho, K.-C. Recent progress in organic sensitizers for dye-sensitized solar cells. *RSC Adv.* **2015**, *5* (30), 23810−23825.

(5) Loudet, A.; Burgess, K. BODIPY dyes and their derivatives: Syntheses and spectroscopic properties. *Chem. Rev.* **2007**, *107* (11), 4891−4932.

(6) Ge, Y.; O'Shea, D. F. Azadipyrromethenes: from traditional dye chemistry to leading edge applications. *Chem. Soc. Rev.* **2016**, *45* (14), 3846−3864.

(7) Jiao, L.; Wu, Y.; Wang, S.; Hu, X.; Zhang, P.; Yu, C.; Cong, K.; Meng, Q.; Hao, E.; Vicente, M. G. H. Accessing Near-Infrared-Absorbing BF2-Azadipyrromethenes via a Push-Pull Effect. *J. Org. Chem.* **2014**, *79* (4), 1830−1835.

(8) Wu, Y.; Cheng, C.; Jiao, L.; Yu, C.; Wang, S.; Wei, Y.; Mu, X.; Hao, E. *β*-Thiophene-Fused BF2-Azadipyrromethenes as Near-Infrared Dyes. *Org. Lett.* **2014**, *16* (3), 748−751.

(9) Teets, T. S.; Partyka, D. V.; Updegraff, J. B.; Gray, T. G. Homoleptic, four-coordinate azadipyrromethene complexes of d(10) zinc and mercury. *Inorg. Chem.* **2008**, *47* (7), 2338−2346.

(10) Partyka, D. V.; Deligonul, N.; Washington, M. P.; Gray, T. G. fac-Tricarbonyl rhenium(I) azadipyrromethene complexes. *Organometallics* **2009**, *28* (20), 5837−5840.

(11) Lu, H.; Mack, J.; Yang, Y.; Shen, Z. Structural modification strategies for the rational design of red/NIR region BODIPYs. *Chem. Soc. Rev.* **2014**, *43* (13), 4778−4823.

(12) Senevirathna, W.; Sauve, G. Introducing 3D conjugated acceptors with intense red absorption: homoleptic metal(ii) complexes of di(phenylacetylene) azadipyrromethene. *J. Mater. Chem. C* **2013**, *1* (40), 6684−6694.

(13) Nabeshima, T.; Yamamura, M.; Richards, G. J.; Nakamura, T. Design and synthesis of dipyrrin complexes bearing unique structures, properties and functions. *Yuki Gosei Kagaku Kyokaishi* **2015**, *73* (11), 1111−1119.

(14) Maar, R. R.; Gilroy, J. B. Group 13 Complexes of Chelating N2 O2(n-) Ligands as Hybrid Molecular Materials. *Chem. - Eur. J.* **2018**, *24* (48), 12449−12457.

(15) Antina, E. V.; Bumagina, N. A. Tetraaryl-substituted aza-BODIPY: synthesis, spectral properties, and possible applications (microreview). *Chem. Heterocycl. Compd.* **2017**, *53* (1), 39−41.

(16) Killoran, J.; Allen, L.; Gallagher, J. F.; Gallagher, W. M.; O'Shea, D. F. Synthesis of BF2 chelates of tetraarylazadipyrromethenes and evidence for their photodynamic therapeutic behaviour. *Chem. Commun.* **2002**, *17*, 1862−1863.

(17) Loudet, A.; Bandichhor, R.; Burgess, K.; Palma, A.; McDonnell, S. O.; Hall, M. J.; O'Shea, D. F. B,O-Chelated azadipyrromethenes as near-IR probes. *Org. Lett.* **2008**, *10* (21), 4771−4774.

(18) Kovtun, Y.; Yakubovskiy, V.; Shandura, M. Azadipyrromethene dye with a fully chelated boron atom. *Chem. Heterocycl. Compd.* **2008**, *44* (10), 1298−1299.

(19) Senevirathna, W.; Liao, J.-y.; Mao, Z.; Gu, J.; Porter, M.; Wang, C.; Fernando, R.; Sauvé, G. Synthesis, characterization and photovoltaic properties of azadipyrromethene-based acceptors: effect of pyrrolic substituents. *J. Mater. Chem. A* **2015**, *3* (8), 4203−4214.

(20) Shi, Z.; Han, X.; Hu, W.; Bai, H.; Peng, B.; Ji, L.; Fan, Q.; Li, L.; Huang, W. Bioapplications of small molecule Aza-BODIPY: from rational structural design to in vivo investigations. *Chem. Soc. Rev.* **2020**, *49* (21), 7533−7567.

(21) Bessette, A.; Hanan, G. S. Design, synthesis and photophysical studies of dipyrromethene-based materials: insights into their applications in organic photovoltaic devices. *Chem. Soc. Rev.* **2014**, *43* (10), 3342−3405.

(22) Leblebici, S. Y.; Catane, L.; Barclay, D. E.; Olson, T.; Chen, T. L.; Ma, B. Near-Infrared Azadipyrromethenes as Electron Donor for Efficient Planar Heterojunction Organic Solar Cells. *ACS Appl. Mater. Interfaces* **2011**, *3* (11), 4469−4474.

(23) Leblebici, S. Y.; Chen, T. L.; Olalde-Velasco, P.; Yang, W.; Ma, B. Reducing exciton binding energy by increasing thin film permittivity: an effective approach to enhance exciton separation efficiency in organic solar cells. *ACS Appl. Mater. Interfaces* **2013**, *5* (20), 10105−10110.

(24) Min, J.; Ameri, T.; Gresser, R.; Lorenz-Rothe, M.; Baran, D.; Troeger, A.; Sgobba, V.; Leo, K.; Riede, M.; Guldi, D. M.; Brabec, C. J. Two similar near-Infrared (IR) absorbing benzannulated aza-BODIPY dyes as near-IR sensitizers for ternary solar cells. *ACS Appl. Mater. Interfaces* **2013**, *5* (12), 5609−5616.

(25) Fan, G.; Yang, L.; Chen, Z. Water-soluble BODIPY and aza-BODIPY dyes: synthetic progress and applications. *Front. Chem. Sci. Eng.* **2014**, *8* (4), 405−417.

(26) Wu, D.; Duran-Sampedro, G.; O'Shea, D. F. Synthesis and properties of water-soluble 1,9-dialkyl-substituted BF_2 azadipyrromethene fluorophores. *Front. Chem. Sci. Eng.* **2020**, *14* (1), 97−104.

(27) Zangade, S.; Mokle, S. An efficient and operationally simple synthesis of some new chalcones by using grinding technique. *Chem. Sci. J.* **2011**, *2* (1), CSJ−13.

(28) Rogers, M. A. T. 2:4-Diarylpyrroles. Part I. Synthesis of 2:4-diarylpyrroles and 2:2′: 4:4′-tetra-arylaxadipyrrornethines. *J. Chem. Soc.* **1943**, *0*, 590−596.

(29) Sworakowski, J.; Janus, K. On the reliability of determination of energies of HOMO levels in organic semiconducting polymers from electrochemical measurements. *Org. Electron.* **2017**, *48*, 46−52.

(30) Bredas, J.-L. Mind the gap! *Mater. Horiz.* **2014**, *1* (1), 17−19.

(31) Löwdin, P. O. On the non-orthogonality problem connected with the use of atomic wave functions in the theory of molecules and crystals. *J. Chem. Phys.* **1950**, *18* (3), 365−375.

(32) Martin, R. L. Natural transition orbitals. *J. Chem. Phys.* **2003**, *118* (11), 4775−4777.

(33) Ivri, J.; Burshtein, Z.; Miron, E. Characteristics of 1, 1′,3,3,3′,3′-hexamethylindotricarbocyanine iodide as a tunable dye laser in the near infrared. *Appl. Opt.* **1991**, *30*, 2484−2488.

(34) Rurack, K.; Spieles, M. Fluorescence quantum yields of a series of red and near-infrared dyes emitting at 600−1000 nm. *Anal. Chem.* **2011**, *83* (4), 1232−1242.

(35) A Guide to Recording Fluorescence Quantum Yields. https://static.horiba.com/fileadmin/Horiba/Application/Materials/Material_Research/Quantum_Dots/quantumyieldstrad.pdf.

(36) Pracht, P.; Bohle, F.; Grimme, S. Automated exploration of the low-energy chemical space with fast quantum chemical methods. *Phys. Chem. Chem. Phys.* **2020**, *22* (14), 7169−7192.

(37) Grimme, S. Exploration of chemical compound, conformer, and reaction space with meta-dynamics simulations based on tight-binding quantum chemical calculations. *J. Chem. Theory Comput.* **2019**, *15* (5), 2847−2862.

(38) Spicher, S.; Grimme, S. Robust atomistic modeling of materials, organometallic, and biochemical systems. *Angew. Chem., Int. Ed.* **2020**, *59* (36), 15665−15673.

(39) Tao, J.; Perdew, J. P.; Staroverov, V. N.; Scuseria, G. E. Climbing the density functional ladder: nonempirical meta-generalized gradient approximation designed for molecules and solids. *Phys. Rev. Lett.* **2003**, *91* (14), 146401.

(40) Grimme, S.; Ehrlich, S.; Goerigk, L. Effect of the damping function in dispersion corrected density functional theory. *J. Comput. Chem.* **2011**, *32* (7), 1456−1465.

(41) Grimme, S.; Antony, J.; Ehrlich, S.; Krieg, H. A consistent and accurate ab initio parametrization of density functional dispersion correction (DFT-D) for the 94 elements H-Pu. *J. Chem. Phys.* **2010**, *132* (15), 154104.

(42) Weigend, F.; Ahlrichs, R. Balanced basis sets of split valence, triple zeta valence and quadruple zeta valence quality for H to Rn: Design and assessment of accuracy. *Phys. Chem. Chem. Phys.* **2005**, *7* (18), 3297−3305.

(43) Dunlap, B. I.; Connolly, J. W. D.; Sabin, J. R. On some approximations in applications of Xα theory. *J. Chem. Phys.* **1979**, *71* (8), 3396−3402.

(44) Weigend, F. Accurate Coulomb-fitting basis sets for H to Rn. *Phys. Chem. Chem. Phys.* **2006**, *8* (9), 1057−1065.

(45) Barone, V.; Cossi, M. Quantum Calculation of Molecular Energies and Energy Gradients in Solution by a Conductor Solvent Model. *J. Phys. Chem. A* **1998**, *102*, 1995−2001.

(46) Najibi, A.; Goerigk, L. The nonlocal kernel in van der waals density functionals as an additive correction: an extensive analysis with special emphasis on the B97M-V and omegaB97M-V approaches. *J. Chem. Theory Comput.* **2018**, *14* (11), 5725−5738.

(47) Chai, J. D.; Head-Gordon, M. Long-range corrected hybrid density functionals with damped atom-atom dispersion corrections. *Phys. Chem. Chem. Phys.* **2008**, *10* (44), 6615−6620.

(48) Neese, F.; Wennmohs, F.; Hansen, A. Efficient and accurate local approximations to coupled-electron pair approaches: An attempt to revive the pair natural orbital method. *J. Chem. Phys.* **2009**, *130* (11), 114108.

(49) Neese, F.; Wennmohs, F.; Becker, U.; Riplinger, C. The ORCA quantum chemistry program package. *J. Chem. Phys.* **2020**, *152* (22), 224108.

(50) Plasser, F. TheoDORE: A toolbox for a detailed and automated analysis of electronic excited state computations. *J. Chem. Phys.* **2020**, *152* (8), No. 084108.

(51) Li, J.; He, J. Synthesis of sequence-regulated polymers: alternating polyacetylene through regioselective anionic polymerization of butadiene derivatives. *ACS Macro Lett.* **2015**, *4* (4), 372−376.